DOI: 10.1070/RCR4741

Innovative oxide materials for electrochemical energy conversion and oxygen separation

Valery V. Belousov

A.A.Baikov Institute of Metallurgy and Materials Science, Russian Academy of Sciences
Leninsky prosp. 49, 119334 Moscow, Russian Federation

Ion-conducting solid metal oxides are widely used in high-temperature electrochemical devices for energy conversion and oxygen separation. However, liquid metal oxides possessing unique electrochemical properties still remain of limited use. The review demonstrates the potential for practical applications of molten oxides. The transport properties of molten oxide materials are discussed. The emphasis is placed on the chemical diffusion of oxygen in the molten oxide membrane materials for electrochemical energy conversion and oxygen separation. The thermodynamics of these materials is considered. The dynamic polymer chain model developed to describe the oxygen ion transport in molten oxides is discussed. Prospects for further research into molten oxide materials are outlined.
The bibliography includes 145 references.

Contents

I. Introduction 934
II. Thermodynamics of molten oxide materials 935
III. Molten oxide layer on metal. Catastrophic oxidation of copper 937
IV. Molten oxide membranes 940
V. Molten oxide fuel cells 945
VI. Modelling. The dynamic polymer chain model 946

I. Introduction

Continuous increase in electricity production by combustion of fossil fuels led to severe environment pollution and depletion of natural resources. According to International Energy Agency (IEA) and other informed circles, fossil fuels will remain the main energy source until the mid-21st century.[1] In this connection, the role of alternative energy sources (nuclear energy, solar energy, wind energy, hydroelectric energy and biomass energy) increases. Traditionally, electrochemical power engineering is of great importance.[2] Electrochemical methods for power generation and electric energy storage are efficient and environmentally friendly. In the nearest future, the energy market share of such electrochemical devices as fuel cells, batteries, accumulators, oxygen separators, electrolyzers, *etc*. will increase. Progress in electrochemical power engineering will be to a great extent determined by advances in functional materials. In this connection, a particular role is assigned to oxygen-ion-conducting oxide materials.[3–5]

V.V.Belousov. Doctor of Physical and Mathematical Sciences, Head of Department of Functional Ceramics, IMET RAS.
Telephone: +7(495)114–5419, e-mail: vbelousov@imet.ac.ru
Current research interests: electrical and mass transport processes in oxide materials with developed surface, high-temperature oxidation of metals.

Received 6 April 2016
Translation: A.M.Raevskiy

At present, the most intensive research avenues include ceramic oxide materials for intermediate- and low-temperature solid-oxide fuel cells and ion transport membranes,[6–13] as well as liquid oxide materials for intermediate-temperature molten oxide fuel cells and molten oxide membranes.[14] Molten oxide fuel cells represent a novel type of fuel cells for electrochemical energy conversion; they combine the advantages of solid-oxide (air as cathode gas) and molten carbonate (highly conductive liquid electrolyte) fuel cells.[15,16] Molten oxide membranes represent an innovative type of ion transport membranes for separation of ultrahigh-purity oxygen from air.[17]

A molten oxide material is a composite consisting of solid grains and liquid channels at grain boundaries that form the so-called liquid-channel grain-boundary structure (LGBS).[18] Intergranular liquid channels provide the molten oxide material with high ionic conductivity, gas tightness and ductility. The LGBS molten oxide materials are usually prepared in two steps, *viz*., by sintering a ceramic composite of specified composition followed by the formation of the LGBS in the ceramic composite by grain boundary wetting.[19] Simple methods for preparation and unique electrochemical and mechanical properties of such materials offer great prospects for technological applications. The LGBS with high mixed ionic-electronic conductivity was for the first time found in the oxide layer formed on copper surface during catastrophic oxidation of copper contacting a low-melting oxide.[20] Accelerated transport of oxygen ions along

© 2017 Russian Academy of Sciences and Turpion Ltd.

intergranular liquid channels led to catastrophic degradation of the metal.

Recently, there has been visible progress in understanding the mechanism of oxygen ion transport in molten oxides. This was facilitated by the following two factors:

— improvement of experimental methods in order to perform highly accurate measurements of oxygen permeability in chemically harsh molten oxides at different temperatures and partial pressures of oxygen;[21] and

— constructing models for correct description of oxygen ion transport in molten oxides.[22]

The development of ideas about the mechanisms of oxygen ion transport in molten oxides makes it possible to design new-generation electrochemical materials and thus improve the efficiency of devices for electrochemical energy conversion and oxygen separation. The aim of this review is to integrate the results of experimental and theoretical research into the title field obtained in the last decade with particular attention paid to chemical diffusion of oxygen in molten oxides.

II. Thermodynamics of molten oxide materials

II.1. Wetting of grain boundaries

The preparation of molten oxide materials includes sintering of ceramic composites followed by the formation of the LGBS (see above). Usually, the LGBS is formed in binary oxide systems described by simple eutectic phase diagrams. To prepare a ceramic composite, a two-phase powder mixture of specified composition is pressed and sintered at a temperature below the eutectic point. Then, the sintered ceramic composite is heated above the eutectic temperature (two-phase region of a corresponding phase diagram, where the solid and liquid phases are in equilibrium). As the ceramic composite is heated at the eutectic temperature, a grain boundary wetting transition occurs and the LGBS is formed, *i.e.*, a molten oxide material with the LGBS is formed. The material consists of solid grains and liquid intergranular channels. Wetting plays an important role in the fabrication of molten oxide materials and we will consider the phenomenon in more detail. Let us describe wetting using Young's equation

$$\gamma_{s/g} = \gamma_{s/l} + \gamma_{l/g}\cos\theta \qquad (1)$$

where $\gamma_{s/g}$, $\gamma_{s/l}$, $\gamma_{l/g}$ are the specific energies at the solid/gas, solid/liquid and liquid/gas interfaces, respectively, and θ is the contact angle. The angle θ varies around zero at the wetting transition; therefore, wetting is referred to as a critical phenomenon. Cahn[23] showed that the wetting transition occurs in the vicinity of the critical point. He considered a two-component liquid $\tau + \beta$ contacting a solid phase (ν); in such a liquid, the two-phase region is confined by the binodal $APCP'A'$ with a critical point C (Fig. 1). At $T \to T_{cr}$, the interface energy $\gamma_{\tau/\beta}$ decreases faster than the interface energy difference $\gamma_{\tau/\nu} - \gamma_{\beta/\nu}$. Consequently, there exists the temperature T_{tr} such that a liquid film of the β-phase is formed between the vessel wall ν and the liquid phase τ above T_{tr}; in other words, a wetting transition (PP' conode) occurs at the temperature T_{tr}. Cahn also showed that the liquid film of the β-phase can exist outside the two-phase region $\tau+\beta$ (between the line PC' and the binodal segment PC) and called this phenomenon the prewetting transition. Cahn's theory[24] was many times confirmed experimentally.

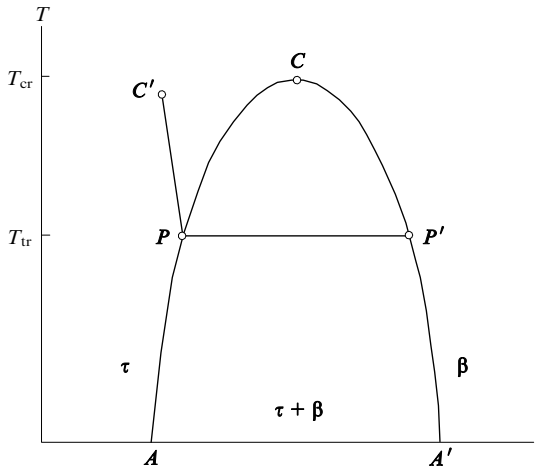


Figure 1. Solubility diagram of a binary system with a limited mutual solubility of components.

A wetting transition can be either first- or second-order[25] and occur without participation of the third phase ν. For instance, liquid films of the β-phase can exist at the grain boundaries of the ceramic (polycrystalline) α-phase if

$$\gamma_{gb} \geqslant 2\gamma_{\alpha/\beta} \qquad (2)$$

where γ_{gb} is the specific grain boundary energy of the α-phase, which depends on the degree of misorientation of the crystalline grains, and $\gamma_{\alpha/\beta}$ is the specific energy of the solid phase (α)/liquid phase (β) interface. The virtual critical point C should be located higher than the solidus line in the corresponding binary phase diagram. With respect to the degree of misorientation there are high-angle and low-angle grain boundaries. Experiments showed that wetting transitions at high-angle grain boundaries in ceramic composites occur at the eutectic point.[26–33] A further heating may lead to wetting of low-angle grain boundaries with a chemically compatible liquid.[34] Let us evaluate the energy $\gamma_{\alpha/\beta}$ corresponding to the wetting of low-angle grain boundaries. Since these grain boundaries are formed by walls of edge dislocations or screw dislocations, their energy is comparable with the energy of dislocations per unit area of grain boundary,[35]

$$\gamma_{gb} = \gamma_0\Psi(\varphi - \ln\Psi) \qquad (3)$$

where γ_0 and φ are the parameters of the model used and Ψ is the grain misorientation angle. According to Eqn (3), γ_{gb} increases with Ψ and reaches a maximum value, $\gamma_{gb(max)}$. Having denoted the angle Ψ corresponding to $\gamma_{gb(max)}$ as Ψ_{max}, one can write Eqn (3) in the form[36]

$$\frac{\gamma_{gb}}{\gamma_{gb(max)}} = \frac{\Psi}{\Psi_{max}}\left(1 - \ln\frac{\Psi}{\Psi_{max}}\right) \qquad (4)$$

According to calculations using expression (4) for $10'' \leqslant \Psi \leqslant 1^\circ$, $\Psi_{max} = 30^\circ$ and $\gamma_{gb(max)} = 10^3$ mJ m^{-2}, the energy of the low-angle grain boundaries in oxide ceramic materials can vary in the range $1 \leqslant \gamma_{gb} \leqslant 150$ mJ m^{-2}. Therefore, the thermodynamic condition for wetting of low-angle grain boundaries [see Eqn (2)] is met at

$0.5 \leqslant \gamma_{\alpha/\beta} \leqslant 75$ mJ m^{-2}. Note that these $\gamma_{\alpha/\beta}$ values are typical of lyophilic colloidal systems.[37]

The aforesaid suggests that wetting of grain boundaries in oxide ceramic composites with a chemically compatible liquid can occur in the two-phase region of corresponding phase diagram, where the solid and liquid phases are in equilibrium. The grain boundary energies vary over a wide range; therefore, the wetting transition temperature will also be different, namely, the lower the grain boundary energy the higher the wetting transition temperature and *vice versa*.

II.2. Intergranular wetting films

Clarke[38] evaluated the equilibrium thickness of intergranular wetting films in ceramic materials. He proposed two approaches within the framework of continuum approximation. One of them is based on evaluation of the grain boundary energies while the other is based on the balance of forces acting along the normal to the grain boundary. The results obtained suggest the existence of a stable thickness ($h \approx 1$ nm, Fig. 2) of the intergranular film. According to Clarke, the equilibrium thickness of intergranular wetting film depends on two competing forces, that is, attractive force due to van der Waals dispersion interaction between grains, which tends to decrease the thickness of the intergranular liquid film, and repulsive force due to the structural (or steric) force of the liquid.

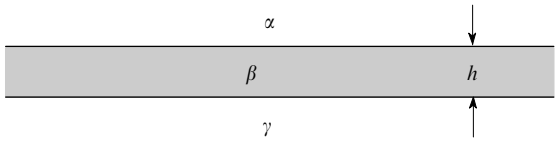


Figure 2. The boundary phase β of thickness h between the phases α and γ: a schematic.

In other words, the equilibrium thickness of an intergranular wetting film is governed by the balance between the long-range and short-range forces. The corresponding balance equation can be written as follows:

$$P + P_c + \Pi = 0 \tag{5}$$

where P is the external pressure, P_c is the capillary pressure and Π is the disjoining pressure (the total pressure due to all interfacial forces acting across the liquid intergranular film[39,40]). To a first approximation, the disjoining pressure is represented by the sum

$$\Pi = \Pi_{disp} + \Pi_{sr} \tag{6}$$

where Π_{disp} is the contribution of the van der Waals dispersion forces and Π_{sr} is that of the structural or steric forces. Thus, the equation for the total normal force acting across the liquid intergranular film has the form

$$P + P_c + \Pi_{disp} + \Pi_{sr} = 0 \tag{7}$$

II.2.a. The dispersion force

In the interaction between individual atoms or molecules the dispersion force is inversely proportional to the seventh power of the interatomic (intermolecular) distance, thus being short-range. The force of dispersion interaction between bulk solid phases is long-range.[41] In order to calculate the London dispersion force acting between two interacting phases separated by a third phase, Dzyaloshinskii *et al.*[42] used an approach based on the Lifshitz quantum field theory and led to the following equation:

$$\Pi_{disp} = \frac{\hbar}{8\pi^2 h^3} \int_0^\infty \sum_{n=1}^{\infty} \frac{1}{n^3} \left[\left(\frac{\varepsilon_\alpha - \varepsilon_\beta}{\varepsilon_\alpha + \varepsilon_\beta} \right) \left(\frac{\varepsilon_\gamma - \varepsilon_\beta}{\varepsilon_\gamma + \varepsilon_\beta} \right) \right] d\xi \tag{8}$$

where $\varepsilon_j = \varepsilon_j(i\xi)$ is the dielectric constant of the jth phase, which depends on the imaginary frequency $i\xi$, and $\hbar$ is the Planck constant.

Equation (8) shows that the dispersion force can be either attractive or repulsive depending on the dielectric constants of the three phases under study (repulsive dispersion force acts if $\varepsilon_\alpha > \varepsilon_\beta > \varepsilon_\gamma$, see Fig. 2). In our case (same-phase grains, *i.e.*, $\varepsilon_\gamma = \varepsilon_\alpha$), Eqn (8) is simplified:

$$\Pi_{disp} = \frac{\hbar}{8\pi^2 h^3} \int_0^\infty \sum_{n=1}^{\infty} \frac{1}{n^3} \left(\frac{\varepsilon_\alpha - \varepsilon_\beta}{\varepsilon_\alpha + \varepsilon_\beta} \right)^2 d\xi = \frac{H_{\alpha\beta\alpha}}{6\pi h^3} \tag{9}$$

where $H_{\alpha\beta\alpha}$ is the Hamaker constant. In this symmerical case, the dispersion force is attractive irrespective of the nature of the grain boundary material.

Therefore, if no external stress is applied to the system and in the absence of capillary pressure, thin intergranular films are unstable against the attractive force due to the dispersion interaction unless there exists a repulsive steric force of sufficient strength to balance the long-range van der Waals force.

II.2.b. The structural component of the disjoining pressure

Taking account of the fact that the structure of the intergranular liquid film of microscopically small thickness is characterized by fluctuating orientational order near each crystalline grain (epitaxy) and using the mean field approximation where orientational ordering across the grain boundary is described by a scalar quantity $\omega(x)$, Clarke[38] proposed to determine the free energy density (g) of the liquid phase as a Taylor expansion

$$g = g_0 + [a\omega^2(x) + b\omega^3(x) + c\omega^4(x) + \ldots] + \lambda \left(\frac{d\omega(x)}{dx} \right)^2 \tag{10}$$

This expression is known as the Ginzburg–Landau or Cahn–Hilalrd equation[43,44] and includes three dominant terms. The first, g_0, is the free energy density of bulk random liquid; the second term is a power series expansion of the order parameter ω (Landau expansion); and the third term, the so-called gradient energy, describes the contribution due to the interaction between adjacent molecules. From the symmetry of the grain-boundary region and, therefore, the order parameter, it follows that $b = 0$. The constant c is small compared to a so that the term ω^4 can be neglected. As a result, Eqn (10) is simplified and one gets

$$g = g_0 + a\omega^2(x) + \lambda \left(\frac{d\omega(x)}{dx} \right)^2 \tag{11}$$

The functional of the excess free energy per unit area of grain boundary is given by

$$\Delta G = \int_{-h/2}^{+h/2} (g - g_0)\mathrm{d}x \tag{12}$$

After the function minimizing this functional (ΔG_{eq}) has been defined, the structural contribution to the disjoining pressure is calculated using the equation

$$\Pi_{sr} = \frac{\mathrm{d}(\Delta G_{eq})}{\mathrm{d}h} \tag{13}$$

To determine the equilibrium thickness of the intergranular liquid film, one should establish the conditions under which the excess free energy functional is minimum. One has to solve the following equation:

$$\Delta G_{eq} = 2\sqrt{(a\lambda)}\omega_0^2 \operatorname{cth}\left(\frac{\sqrt{a/\lambda}\,h}{2}\right) \tag{14}$$

provided that crystalline grains are misoriented in such a manner that the first monolayers of the liquid film are oriented in opposite directions, *i.e.*,

$$\omega_0 = \omega\frac{h}{2} = -\omega\left(-\frac{h}{2}\right) \tag{14a}$$

Substituting Eqn (14) into formula (13), one gets the expression for the disjoining pressure:

$$\Pi_{sr} = \frac{\mathrm{d}(\Delta G_{eq})}{\mathrm{d}h} = -\frac{\phi_0}{\mathrm{sh}^2(h/2\xi)} \tag{15}$$

where $\phi_0 = a\omega_0^2$ and $\xi = \sqrt{\lambda/a}$ is the correlation length. At $h > \xi$, the contribution of the disjoining pressure can be evaluated using the expression

$$\Pi_{sr} = -4\phi_0 \exp\left(-\frac{h}{\xi}\right) \tag{16}$$

This model predicts a repulsive character of the structural disjoining pressure, as required to balance the attractive intergranular force originated from the van der Waals dispersion interaction. Substituting Eqns (9) and (16) into Eqn (7), one gets the equation of balance in the form

$$P + P_c + \frac{H_{\alpha\beta\alpha}}{6\pi h^3} - 4a\omega_0^2 \exp\left(-\frac{h}{\xi}\right) = 0 \tag{17}$$

The equilibrium thickness of the intergranular liquid film can be determined from

$$\frac{H_{\alpha\beta\alpha}}{6\pi h^3} = 4a\omega_0^2 \exp\left(-\frac{h}{\xi}\right) \tag{18}$$

Using the continuum approach based on the balance of forces acting along the normal to the intergranular liquid film, Clarke showed that such films may have the equilibrium thickness. The thickness of the intergranular film calculated using formula (18) is close to experimental data

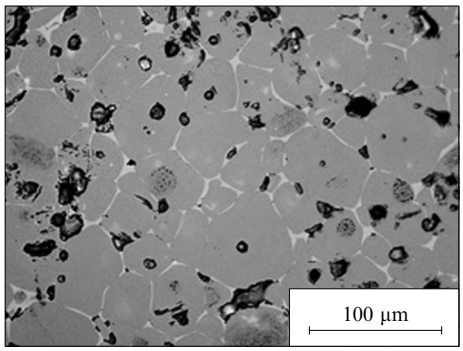


Figure 3. A photograph of intergranular films in a ceramic composite MgO – 12 mass % Mg_2TiO_4 (fracture face).
From materials collected during the preparation of manuscript.[28]

($\sim$1 nm). However, this contradicts the data reported by Derjaguin,[39,40] who demonstrated that on the length scale less than 1.5 nm the continuum approach is of limited use and therefore quantitative estimates are not reliable. Besides, experiments with ceramic materials confirmed the existence of intergranular wetting films whose thickness much exceeds that predicted by Clarke (Fig. 3). Note that the nature of the nanometre-thick intergranular films in ceramic materials is unclear at the moment. Thus, one should clarify whether such films are truly wetting, prewetting or adsorption ones.

In conclusion, recall that grain boundary wetting transitions and formation of the LGBS can occur in ceramic oxide composites at the eutectic point. Intergranular liquid channels provide the molten oxide materials with LGBS high ionic conductivity, gas tightness and ductility. As will be shown below, such a combination of unique properties of these materials offers great prospects for their application in electrochemical devices for power generation and production of oxygen.

III. Molten oxide layer on metal. Catastrophic oxidation of copper

The LGBS with high oxygen ion conductivity was for the first time discovered in the oxide layer formed on copper surface during catastrophic oxidation of copper contacting low-melting oxides Bi_2O_3, V_2O_5 or MoO_3.[20] Rapid transport of oxygen along intergranular liquid channels led to catastrophic degradation of the metal. However, rapid mass transfer can be successfully used in practice electrochemical devices such as molten oxide fuel cells and molten oxide membranes. Therefore, studies on the mechanism of the catastrophic oxidation of metals are of importance for the design of innovative molten oxide LGBS materials with high oxygen ion conductivity. Accelerated oxidation of metals and alloys due to formation of a liquid corrosion product has been widely discussed in the literature.[45–62] Consider the mechanism of catastrophic oxidation of copper taking the best studied system Cu – Bi_2O_3 as an example.

The catastrophic oxidation of copper coated with a Bi_2O_3 layer includes two stages, a fast and a superfast one.[45,46] The fast stage is realized under a thin (10 – 100 μm) Bi_2O_3 layer and proceeds by the diffusion mechanism, while the superfast stage is realized under a thick (>1 cm) Bi_2O_3 layer and proceeds by the fluxing

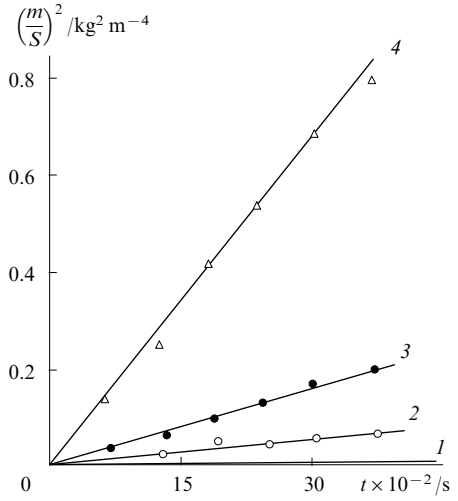


Figure 4. Kinetics of catastrophic oxidation of copper plates (20 × 20 × 0.4 mm) coated with a Bi_2O_3 layer of different thickness at 1073 K.[45]
Film thickness /10^{-5} m: 0.2 (*1*), 3 (*2*), 6 (*3*), 9 (*4*);
$10^5 k''$ /kg^2 m^{-4} s^{-1}: 0.012 (*1*), 1.6 (*2*), 4.9 (*3*), 21 (*4*).

mechanism. Since in the text below we will only be interested in the diffusion mechanism, consider the fast stage of the process in question. It was established that copper plates coated with a thin Bi_2O_3 layer undergo catastrophic oxidation at 1043 K. The kinetics of the process at different thickness of the Bi_2O_3 layer is shown in Fig. 4. The catastrophic oxidation of copper obeys a parabolic rate law and, therefore, is diffusion-controlled

$$\left(\frac{m}{S}\right)^2 = k''t \tag{19}$$

where m is the change in the mass of the oxide layer growing on the metal, S is the surface area of the copper plates, k'' (kg^2 m^{-4} s^{-1}) is the parabolic rate constant, and t is time.

Equation (19) is used only if the mass of the growing oxide layer is controlled. If the thickness of the growing layer is measured, another equation is used:

$$h^2 = 2k't \tag{20}$$

where h is the thickness of the oxide layer growing on the metal and k' is the parabolic rate constant (m^2 s^{-1}).

The oxide layer formed on the copper surface during the catastrophic oxidation process consists of Bi_2CuO_4, CuO, Cu_2O and Bi_2O_3.[45] According to the phase diagram of the Bi_2O_3–CuO system,[63,64] the threshold temperature (1043 K) of the catastrophic oxidation of copper coincides with the Bi_2CuO_4–Bi_2O_3 eutectic point. A grain boundary wetting transition and formation of the LGBS in Bi_2CuO_4–Bi_2O_3 ceramic composites at 1043 K was confirmed experimentally (Fig. 5). Thus, the catastrophic oxidation of copper is related to the formation of the LGBS in the oxide layer.

Studies on the electrochemical properties of LGBS ceramic composites Bi_2CuO_4–(5–20) mass % Bi_2O_3 showed that they are mixed ionic-electronic conductors in which solid Bi_2CuO_4 grains conduct electrons while inter-

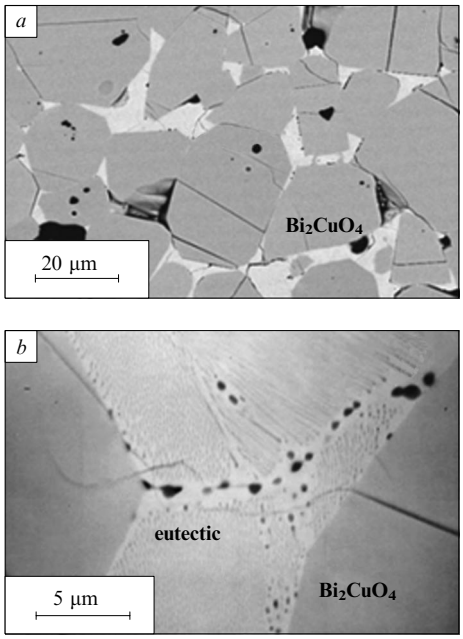


Figure 5. Microstructure (fracture face) of the molten oxide LGBS composite Bi_2CuO_4 — 20 mass % Bi_2O_3 after cooling from 1053 K.[45]
General view (*a*) and intergranular channel (*b*).

granular liquid channels predominantly conduct oxygen ions.[65,66] The ionic conductivity of the composites increases with increasing volume fraction of the liquid phase (Fig. 6). This suggests that the molten oxide layer with the larger volume fraction of the liquid phase, formed on the copper surface, also has a higher oxygen ion conductivity than the oxide layer with the lower content of the liquid phase and, therefore, higher rate of catastrophic oxidation, which was also confirmed experimentally (see Fig. 4).

Consider a theory of the catastrophic oxidation of copper under a thin layer of a low-melting oxide.[67] The

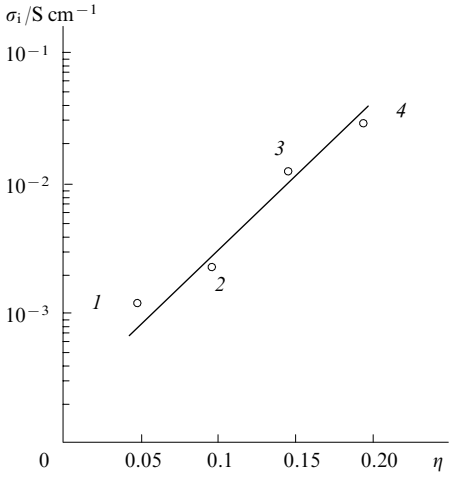


Figure 6. Oxygen ion conductivity of the molten oxide LGBS composites Bi_2CuO_4–5 mass % Bi_2O_3 (*1*), 10 mass % Bi_2O_3 (*2*), 15 mass % Bi_2O_3 (*3*), 20 mass % Bi_2O_3 (*4*) plotted *vs.* volume fraction of the liquid phase (η) at 1073 K.[67]

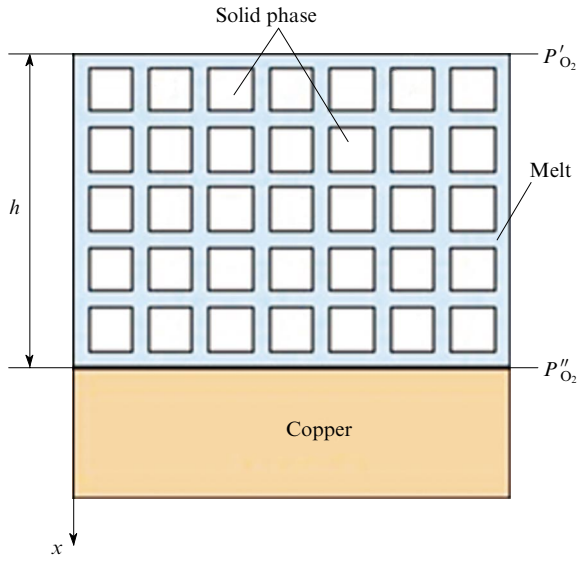


Figure 7. Scheme of an oxide layer formed on copper surface during the catastrophic oxidation of copper.[49]

model structure of the oxide layer used in developing the theory is shown in Fig. 7. The theory was developed under the following assumptions:

— the LGBS is formed in the oxide layer;

— intergranular liquid channels act as pathways for oxygen ion transport;

— the oxidation rate is controlled by the diffusion of oxygen ions;

— oxygen ions and electrons are the most mobile charge carriers;

— transport of ions and electrons across the oxide layer occurs in such a manner that the total electric current is zero;

— a steady state is established throughout the oxide layer;

— the solubility of oxygen in copper is neglected; and

— the thickness of the oxide layer is large compared to the distances at which the space charge effects manifest themselves.

If the oxygen concentration in the oxide layer is designated by c and the layer thickness at instant t is designated by h (see Fig. 7), the mass balance equation takes the form:

$$c\frac{\mathrm{d}h}{\mathrm{d}t} = j_{O_2} \tag{21}$$

where j_{O2} is the oxygen flux through the molten oxide LGBS layer. Usually, diffusion-controlled oxygen flux is described by the Wagner equation. In our case, the action of the chemical potential gradient causes oxygen ions to migrate towards regions with reduced partial pressure of oxygen ($P'_{O_2} > P''_{O_2}$, *i.e.*, through the oxide layer towards the metal). Since oxygen ions are charged, such a migration will produce an electric field and subsequent transport of electrons through the oxide layer in the opposite direction. The relative migration rates of oxygen anions and electrons are balanced, so the total charge transferred through the oxide layer is zero. Charged species (oxygen ions) respond to both the chemical potential gradient and the electric potential gradient. Joint action of these gradients provides the driving force of ion migration, that is, the electrochemical potential gradient. Consider an ion bearing the charge z. At a point characterized by the chemical potential gradient $\partial\mu/\partial x$ and the electric potential gradient $\partial\varphi/\partial x$, the ion experiences the electrochemical force (Q)

$$Q = \frac{1}{N_A}\frac{\mathrm{d}\mu}{\mathrm{d}x} + z\mathrm{e}\frac{\partial\varphi}{\partial x} \tag{22}$$

where N_A is the Avogadro constant and e is the electron charge. The ion moving under the action of a constant force acquires a constant drift velocity. The stabilized drift velocity of the ion under the action of a unit force is characterized by the mobility (B) of a species. Therefore, the oxygen ion flux j_i (mol m^{-2} s^{-1}) is given by

$$j_i = \frac{c_i B_i}{N_A^2 z_i \mathrm{e}}\left(\frac{\mathrm{d}\mu_i}{\mathrm{d}x} + z_i \mathrm{F}\frac{\partial\varphi}{\partial x}\right) \tag{23}$$

where c_i is the concentration of oxygen ions, B_i is the mobility of oxygen ions and F is the Faraday constant. The mobility is related to the ionic conductivity (σ_i):

$$B_i = \frac{\sigma_i}{c_i z_i \mathrm{e}} \tag{24}$$

Substituting Eqn (24) into Eqn (23), one gets the expression for the ion flux:

$$j_i = \frac{\sigma_i}{z_i^2 \mathrm{F}^2}\left(\frac{\mathrm{d}\mu_i}{\mathrm{d}x} + z_i \mathrm{F}\frac{\partial\varphi}{\partial x}\right) \tag{25}$$

Correspondingly, for the electron flux j_e one has

$$j_e = \frac{\sigma_e}{z_e^2 \mathrm{F}^2}\left(\frac{\mathrm{d}\mu_e}{\mathrm{d}x} + z_e \mathrm{F}\frac{\partial\varphi}{\partial x}\right) \tag{26}$$

where σ_e is the electronic conductivity. The electrical neutrality condition has the form

$$z_i j_i = z_e j_e \tag{27}$$

Using Eqns (25)–(27), one can express $\partial\varphi/\partial x$

$$\frac{\partial\varphi}{\partial x} = \frac{1}{\sigma_i + \sigma_e}\left(\frac{\sigma_i}{z_i}\frac{\mathrm{d}\mu_i}{\mathrm{d}x} + \frac{\sigma_e}{z_e}\frac{\mathrm{d}\mu_e}{\mathrm{d}x}\right) \tag{28}$$

Substituting Eqn (28) into Eqn (25) gives the expression for the oxygen ion flux:

$$j_i = \frac{\sigma_i \sigma_e}{z_i^2 \mathrm{F}^2(\sigma_i + \sigma_e)}\left(\frac{\mathrm{d}\mu_i}{\mathrm{d}x} - \frac{z_i}{z_e}\frac{\mathrm{d}\mu_e}{\mathrm{d}x}\right) \tag{29}$$

Taking account of the electron charge ($z_e = -1$) and oxygen ion charge ($z_i = -2$), Eqn (29) can be transformed to

$$j_i = \frac{\sigma_i \sigma_e}{4\mathrm{F}^2(\sigma_i + \sigma_e)}\left(\frac{\mathrm{d}\mu_i}{\mathrm{d}x} - 2\frac{\mathrm{d}\mu_e}{\mathrm{d}x}\right) \tag{30}$$

Using the dissociation equation

$$\frac{1}{2}\mathrm{O}_2 \rightarrow \mathrm{O}^{2-} - 2\mathrm{e}^-, \tag{30a}$$

the chemical potential oxygen is

$$\frac{1}{2}\mu_{O_2} = \mu_i - 2\mu_e \quad (31)$$

Thus, the oxygen ion flux across the oxide layer can be written in the form

$$j_i = \frac{\sigma_i\sigma_e}{8F^2(\sigma_i+\sigma_e)}\frac{d\mu_{O_2}}{dx} \quad (32)$$

where σ_i, σ_e and $d\mu_{O_2}/dx$ are the instantaneous values at a given point of the oxide layer. Since they may vary from one point to another, it is necessary to integrate Eqn (32)

$$j_{O_2} = \frac{1}{2}j_i = \frac{1}{16F^2h}\int_{\mu''_{O_2}}^{\mu'_{O_2}}\sigma_{amb}d\mu_{O_2} \quad (33)$$

where j_{O_2} is the oxygen flux, h is the thickness of the LGBS oxide layer, σ_{amb} is the ambipolar conductivity of oxygen ions and electrons in the oxide layer

$$\sigma_{amb} = \frac{\sigma_i\sigma_e}{\sigma_i+\sigma_e} \quad (34)$$

The chemical potential of oxygen, μ_{O_2}, is related to the partial pressure of oxygen P_{O_2}:

$$\mu_{O_2} = \mu^\circ_{O_2} + RT\ln P_{O_2} \quad (35)$$

where $\mu^\circ_{O_2}$ is the standard chemical potential of oxygen, R is the universal gas constant and T is temperature. Substituting Eqn (35) into Eqn (33), one gets

$$j_{O_2} = \frac{RT}{16F^2h}\int_{\ln P''_{O_2}}^{\ln P'_{O_2}}\sigma_{amb}d\ln P_{O_2} \quad (36)$$

where P'_{O_2} and P''_{O_2} is the partial pressure of oxygen at the air/oxide layer and oxide layer/copper interfaces, respectively (see Fig. 7). Using the average value σ_{amb}, we get

$$j_{O_2} = \frac{RT}{16F^2h}\bar{\sigma}_{amb}\ln\frac{P'_{O_2}}{P''_{O_2}} \quad (37)$$

If $\sigma_e \gg \sigma_i$, Eqn (37) is transformed to

$$j_{O_2} = \frac{RT}{16F^2h}\sigma_i\ln\frac{P'_{O_2}}{P''_{O_2}} \quad (38)$$

The parabolic temporal law of oxidation has the form

$$\frac{dh}{dt} = \frac{k'}{h} \quad (39)$$

Here k' ($m^2\ s^{-1}$) is the parabolic rate constant related to k'' ($kg^2\ m^{-4}\ s^{-1}$) as follows:

$$k' = \frac{V^2}{2A^2}k'' \quad (40)$$

where V is the molar volume of the oxide layer and A is the atomic mass of oxygen. Using Eqns (21), (38), (39) and (40), the rate constant k'' can be expressed as

$$k'' = \frac{RTA^2\sigma_i}{8F^2V^2c}\ln\frac{P'_{O_2}}{P''_{O_2}} \quad (41)$$

The rate constants k'' calculated using expression (41) are in the range between 2.0×10^{-5} and 4.9×10^{-4} $kg^2\ m^{-4}\ s^{-1}$ ($T = 1073$ K, $A^2 = 2.6\times10^{-4}$ $kg^2\ mol^{-2}$, $V^2 = 1.5\times10^{-10}$ $m^6\ mol^{-2}$, $c = 4.0\times10^4$ mol m^{-3}, $P'_{O_2} = 0.021$ MPa, $P''_{O_2} = 0.0001$ MPa, $\sigma_i = 0.14$ and 3.6 S m^{-1}) and coincide in order of magnitude with experimental data ($k'' = 1.6\times10^{-5}$–2.1×10^{-4} $kg^2\ m^{-4}\ s^{-1}$) (see Fig. 4); this indicates a reasonable agreement between theory and experiment.

It should be noted that the mixed-conducting molten oxide LGBS layer found on the copper surface during the catastrophic oxidation of copper[20] served a prototype for the design of novel molten oxide membranes with high mixed oxygen-ion-electronic conductivity.[68]

IV. Molten oxide membranes

IV.1. Materials

Wagner[69] was the first who considered mixed ionic-electronic conductors as practically attractive. If a mixed-conducting material is placed between two gas-filled compartments that differ in the partial pressure of oxygen, the material can act as oxygen separation membrane. More recently, ten Elshof *et al.*[70] proposed a perovskite-related mixed conductor $Sr(Fe,Co)O_{3-\delta}$ as membrane material. Bouwmeester and Burggraaf,[71] as well as Peca and Fierro[72] compiled the results of studies on perovskite-related mixed-conducting membrane materials. Mazanec *et al.*[73] proposed a concept of a two-phase oxygen-permeable composite material. High mixed ionic-electronic conductivity was discovered in the solid electrolyte/noble metal cermets. Cermets YSZ/Pd (where YSZ is yttria-stabilized zirconia),[74] GDC/Pd (where GDC is gadolinium-doped ceria),[75] GDC/Ag,[76] $(Bi_2O_3)_{0.75}(Er_2O_3)_{0.25}$/Ag (Refs 77 and 78) are characterized by rather high oxygen permeability. Also, high oxygen permeability was demonstrated by the ceramic composites δ-Bi_2O_3–In_2O_3 and δ-Bi_2O_3–NiO prepared by *in situ* crystallization of molten Bi_2O_3,[79,80] $Ce_{0.8}Gd_{0.2}O_{2-\delta}$–$Fe_2CoO_4$ (Ref. 81) and $Ce_{0.8}Sm_{0.2}O_{2-\delta}$–$SrCO_3$–$Co_3O_4$ (Ref. 82). Small amounts of transition metal oxides added to a molten slag also significantly improve the oxygen permeability of the slag.[83–85]

Recently, high oxygen permeability of molten oxide LGBS composites based on Bi_2O_3 and V_2O_5 has been reported.[86] These materials seem to be promising as molten oxide membranes[68] for ultrahigh purity oxygen separators. Molten oxide membrane materials can be divided into two groups. One of them contains molten Bi_2O_3 while the other contains molten V_2O_5. High oxygen ion conductivity of these oxides in the molten state was confirmed experimentally.[87] The first group includes the systems NiO–Bi_2O_3, In_2O_3–Bi_2O_3, Co_3O_4–Bi_2O_3, ZnO–Bi_2O_3 and CuO–Bi_2O_3; the second group includes ZrO_2–V_2O_5 and Bi_2O_3–V_2O_5. These membrane materials consist of electron-conducting solid grains (dark areas in Figs 8 and 9) and intergranular liquid channels with predominant oxygen ion conductivity (light areas in Figs 8 and 9). Intergranular

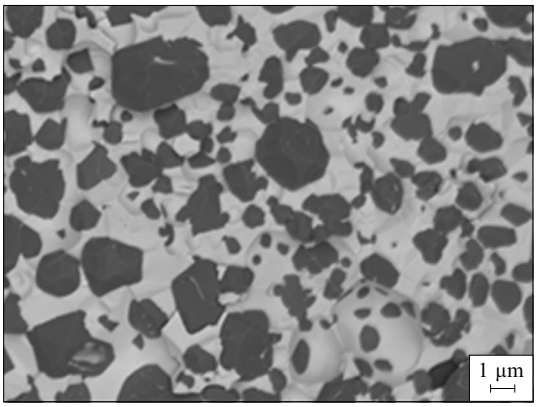


Figure 8. Microstructure (fracture face) of the molten oxide LGBS composite Co_3O_4–36 mass % Bi_2O_3 after cooling from 1123 K.[17]

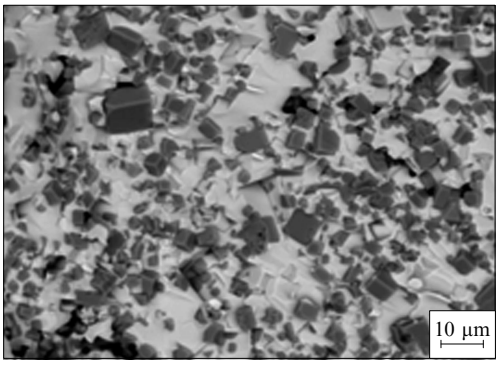


Figure 9. Microstructure (fracture face) of the molten oxide LGBS composite In_2O_3–30 mass % Bi_2O_3 after cooling from 1073 K.[19]

liquid channels provide the membrane material with high ionic conductivity, gas tightness and ductility (Fig. 10).

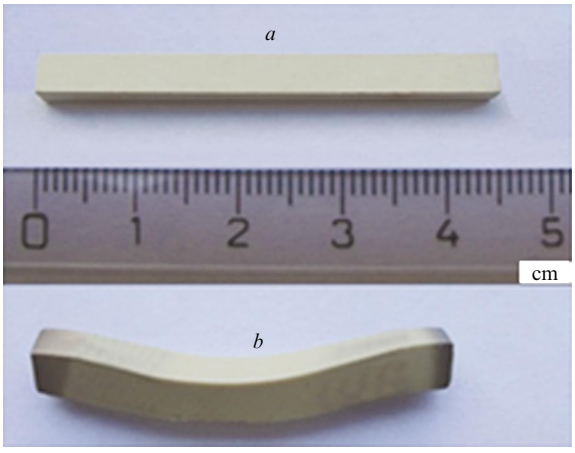


Figure 10. Photograph of the starting ceramic composite ZnO–30 mass % Bi_2O_3 (*a*) and the molten oxide LGBS composite ZnO–30 mass % Bi_2O_3 after deformation at 1073 K (*b*).[19]

IV.2. Electrical conductivity

A number of molten oxide LGBS materials exhibit high mixed ionic-electronic conductivity. The temperature dependence of the conductivity of the composite Co_3O_4–36 mass % Bi_2O_3 is shown in Fig. 11. A large contribution to the total conductivity of the composite comes from Co_3O_4.[88] According to published data,[89,90] the nonlinear temperature dependence of the conductivity of this composite is due to partial structural transition of Co_3O_4 from the normal to the inverse spinel; this seems to be due to the change in the state of electron spins in Co^{3+} (from the low-spin to the high-spin configuration). At 1953 K, a grain boundary wetting transition occurs and the LGBS is formed. Measurements of the oxygen ion transport number in the molten oxide LGBS composite Co_3O_4–36 mass % Bi_2O_3 in the temperature interval 1053–1123 K showed that the material exhibits both electronic conductivity and oxygen ion conductivity, thus being a mixed ionic-electronic conductor.

The conductivity and oxygen ion transport number of the molten oxide LGBS composites Bi_2CuO_4–Bi_2O_3 at 1053 K at different average Bi_2CuO_4 grain size are listed in Table 1.[65,66] As can be seen, the smaller the grain size the higher the ionic conductivity of the composites. Such a correlation can be explained by the contribution of the solid oxide/liquid oxide interfaces to the ionic conductivity of the composites.

The temperature dependences of conductivity of composites ZnO–Bi_2O_3 are shown in Fig. 12. From the phase diagram of the system ZnO–Bi_2O_3 (Refs 92 and 93) it follows that a low-conductive phase $Bi_{38}ZnO_{58}$ with the sillenite structure exists in the temperature interval 873–1026 K and, therefore, the major contribution to the conductivity comes from ZnO.[94] An increase in conductivity at 1026 K is due to the grain boundary wetting transition and formation of the LGBS. The oxygen ion transport number and the conductivity of the molten oxide LGBS composites ZnO–Bi_2O_3 increase with increasing volume fraction of the liquid phase η (Fig. 13).

The conductivity of the composites NiO–Bi_2O_3 and In_2O_3–Bi_2O_3 is plotted *vs.* temperature in Fig. 14. The

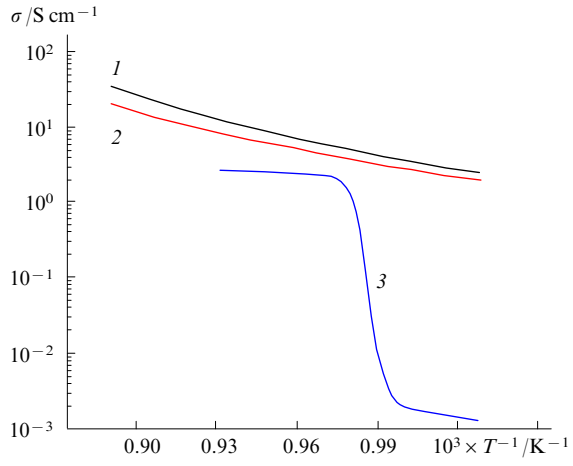


Figure 11. Conductivity of Co_3O_4 (*1*), Co_3O_4–6 mass % Bi_2O_3 (*2*) and Bi_2O_3 (*3*) plotted *vs.* temperature.[17]
Curves *1* and *3* are shown for comparison.

Table 1. Oxygen ion conductivity (σ_i) and transport number (t_i) at different average grain size (d) in the molten oxide LGBS composites $Bi_2CuO_4-Bi_2O_3$ at 1053 K.[65]

Composite	t_i	σ_i /S cm^{-1}	d /μm
Bi_2CuO_4 – 10 mass % Bi_2O_3	0.03	0.22	20
Bi_2CuO_4 – 10 mass % Bi_2O_3	0.05	0.42	10
Bi_2CuO_4 – 15 mass % Bi_2O_3	0.14	1.26	20
Bi_2CuO_4 – 15 mass % Bi_2O_3	0.18	1.68	10
Bi_2CuO_4 – 20 mass % Bi_2O_3	0.26	2.91	20
Bi_2CuO_4 – 20 mass % Bi_2O_3	0.32	6.50	10

electronic conductivity of In_2O_3 and the hole conductivity of NiO are most pronounced in the temperature interval 773–1003 K.[96,97] The conductivity jump at 1003 K is due to the polymorphic transformation α-$Bi_2O_3 \rightarrow \delta$-$Bi_2O_3$, which is accompanied by a significant increase in the oxygen ion conductivity.[98,99] Considerable intrinsic disorder and high mobility of oxygen ions are in agreement with the

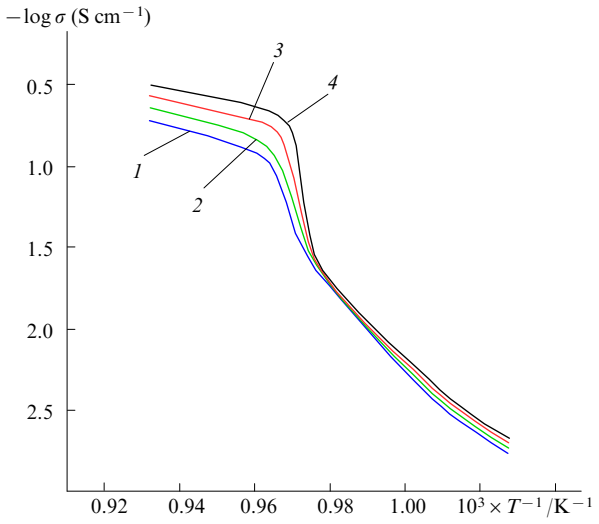


Figure 12. Conductivity of the molten oxide LGBS composites $ZnO-Bi_2O_3$ containing 15 mass % Bi_2O_3 (*1*), 20 mass % Bi_2O_3 (*2*), 25 mass % Bi_2O_3 (*3*) and 30 mass % Bi_2O_3 (*4*) plotted *vs.* temperature.[91]

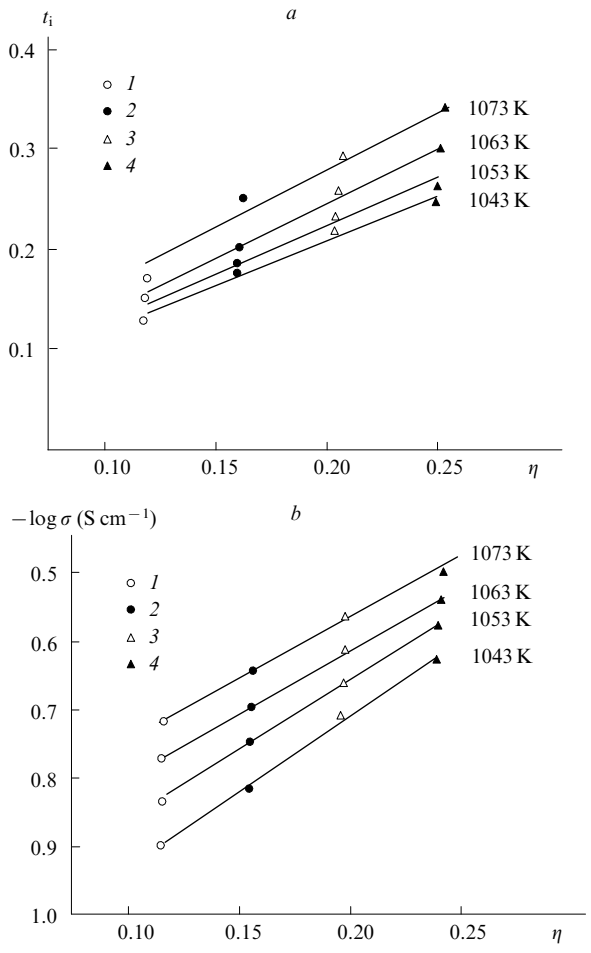


Figure 13. Oxygen ion transport number (*a*) and conductivity (*b*) of the molten oxide LGBS composites $ZnO-Bi_2O_3$ plotted *vs.* volume fraction of the liquid phase at different temperatures.[91]
Bi_2O_3 content (mass %): 15 (*1*), 20 (*2*), 25 (*3*) and 30 (*4*).

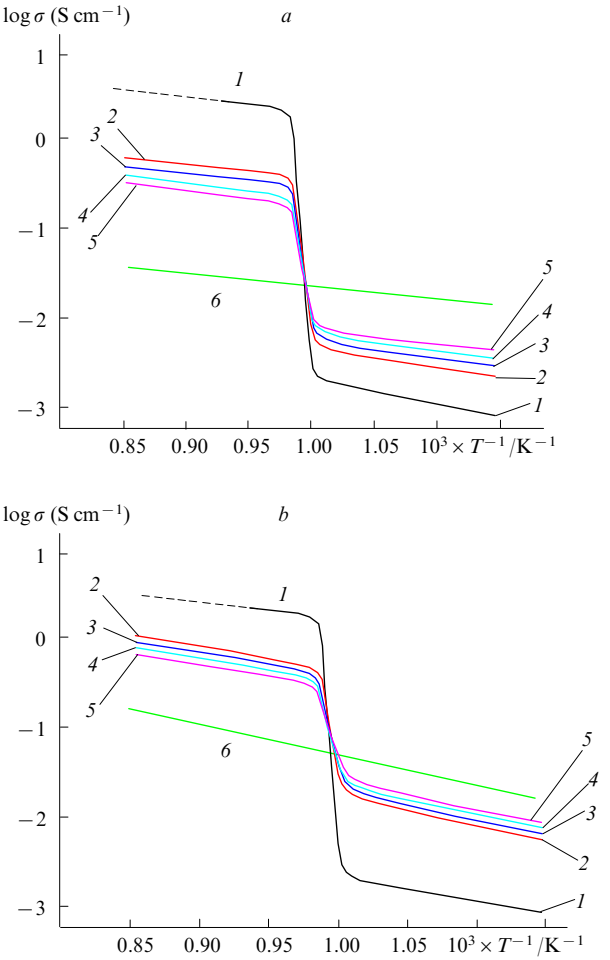


Figure 14. Conductivity of $NiO-Bi_2O_3$ (*a*) and $In_2O_3-Bi_2O_3$ (*b*) composites plotted *vs.* temperature.
Bi_2O_3 content (mass %): 100 (*1*), 48 (*2*), 42 (*3*), 36 (*4*), 30 (*5*) and 0 (*6*).[68,95]

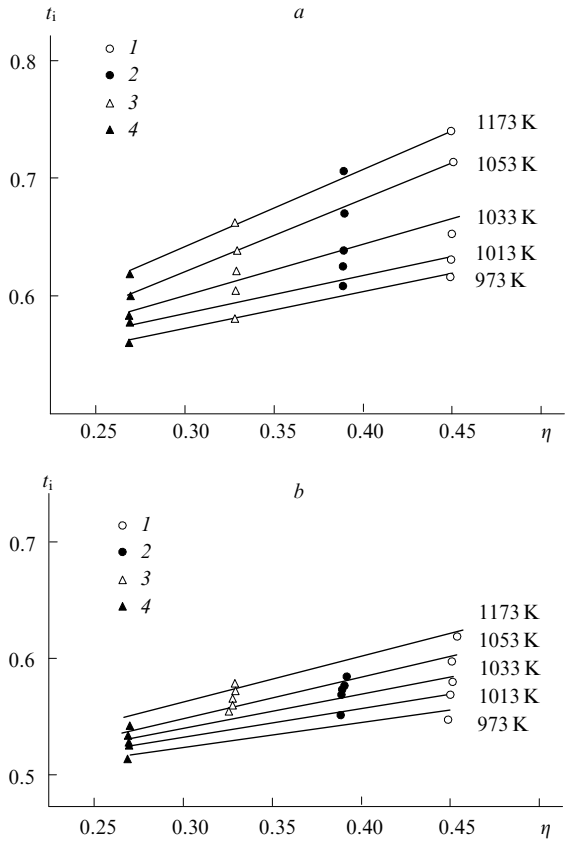


Figure 15. Oxygen ion transport number of the molten oxide LGBS composites $NiO-Bi_2O_3$ (*a*) and $In_2O_3-Bi_2O_3$ (*b*) plotted *vs.* volume fraction of the liquid phase at different temperatures.[68,95]
Bi_2O_3 content (mass %): 48 (*1*), 42 (*2*), 36 (*3*) and 30 (*4*).

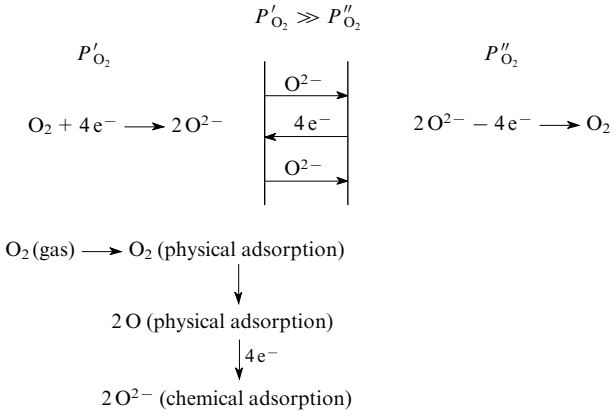


Figure 17. Oxygen ion and electron transport through ion-transport membranes: a schematic.[19]

entropy and structure of δ-Bi_2O_3. For instance, an increase in entropy upon the α-$Bi_2O_3 \rightarrow \delta$-$Bi_2O_3$ transition is ~75% of the total increase in entropy upon transition of solid α-Bi_2O_3 to the liquid state.[100] Hence, the disorder and conductivity of solid δ-Bi_2O_3 are almost comparable with those of liquid Bi_2O_3 and therefore the solid δ-$Bi_2O_3 \rightarrow$ liquid Bi_2O_3 transition at 1093 K is not accompanied by a significant increase in the ionic conductivity. The dependence of the oxygen ion transport number on the volume fraction of the liquid phase in the molten oxide LGBS composites $NiO-Bi_2O_3$ and $In_2O_3-Bi_2O_3$ is presented in Fig. 15. In these systems, only the intergranular liquid channels conduct oxygen ions; therefore, the oxygen ion transport number increases as the volume fraction of the liquid phase increases.[95] The aforesaid is also confirmed by the dependence of the conductivity of the molten oxide LGBS composites $NiO-Bi_2O_3$ and $In_2O_3-Bi_2O_3$ on the volume fraction of the liquid phase (Fig. 16).

In conclusion, mention may be made that the molten oxide LGBS composites considered in this Chapter conduct both oxygen ions and electrons and can thus be used as ion

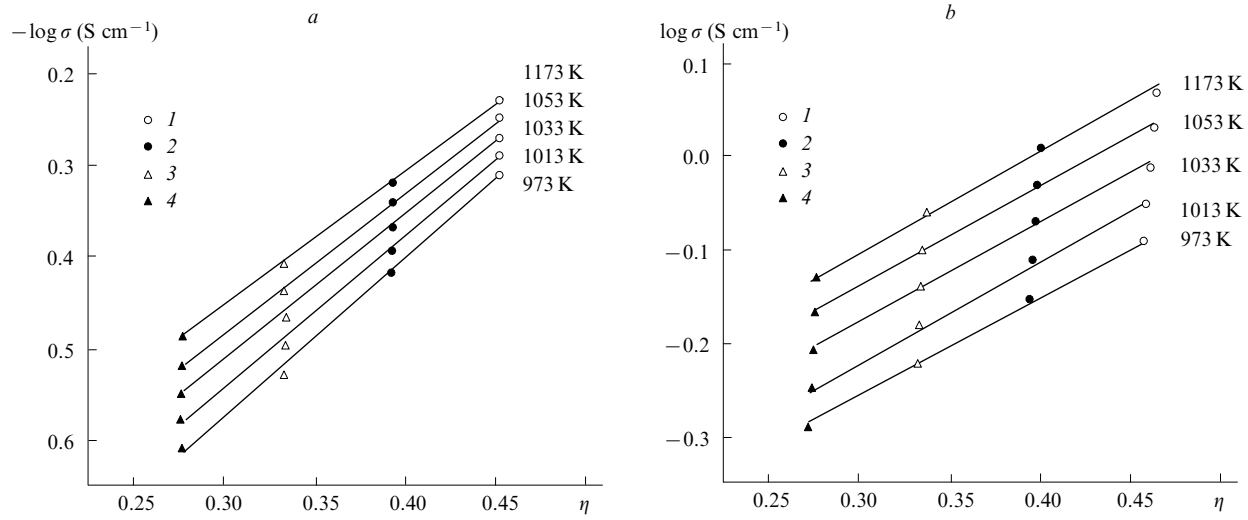


Figure 16. Conductivity of the molten oxide LGBS composites $NiO-Bi_2O_3$ (*a*) and $In_2O_3-Bi_2O_3$ (*b*) plotted *vs.* volume fraction of the liquid phase at different temperatures.[68,95]
Bi_2O_3 content (mass %): 48 (*1*), 42 (*2*), 36 (*3*) and 30 (*4*).

transport membranes for oxygen separation from air. Rapid transport of oxygen through these composites under the action of electrochemical potential gradient is due to high ambipolar oxygen ion and electronic conductivity of these systems (Fig. 17).

IV.3. Gas permeability

Molten oxide LGBS membrane materials exhibit high oxygen permeability.[68] Usually, oxygen transport occurs in three stages. The first stage involves dissociation of oxygen molecules into anions at the air/membrane material interface (see Fig. 17), also known as the surface exchange reaction.[101, 102] In the second stage, oxygen anions migrate through the membrane material; this is the so-called coupled chemical diffusion. The third stage represents recombination of oxygen anions to molecules. Each stage can be rate-limiting for the oxygen transport through the membrane material. To establish the rate-limiting stage, the oxygen flux was measured at different thickness of the membrane material. If the rate of oxygen transport across the membrane is controlled by the chemical diffusion, the oxygen flux should be inversely proportional to the membrane thickness (at specified difference of the partial pressures of oxygen) in accordance with Eqn (37). Linear dependence between the oxygen flux and membrane thickness (in the experimental thickness interval of 0.1–0.3 cm) for the molten oxide LGBS membrane materials $NiO-Bi_2O_3$, $In_2O_3-Bi_2O_3$, $Co_3O_4-Bi_2O_3$ and $ZrV_2O_7-V_2O_5$ indicates that the oxygen transport rate in these materials is diffusion controlled.[68] However, the dependence for the molten oxide LGBS membrane material $BiVO_4-V_2O_5$ is nonlinear (Fig. 18). Consequently, the oxygen transport rate is limited by both chemical diffusion and surface exchange reactions (mixed control).[101] In this case, the oxygen flux can be described by the equation

$$j_{O_2} = \frac{RT}{16F^2(h+2h_c)}\bar{\sigma}_{amb}\ln\frac{P'_{O_2}}{P''_{O_2}} \qquad (42)$$

where h_c is the characteristic membrane thickness at which the oxygen transport rate is equally controlled by the coupled chemical diffusion and by the surface exchange reactions. The characteristic membrane thickness is defined as

$$h_c = t_e\frac{D_i}{K} \qquad (43)$$

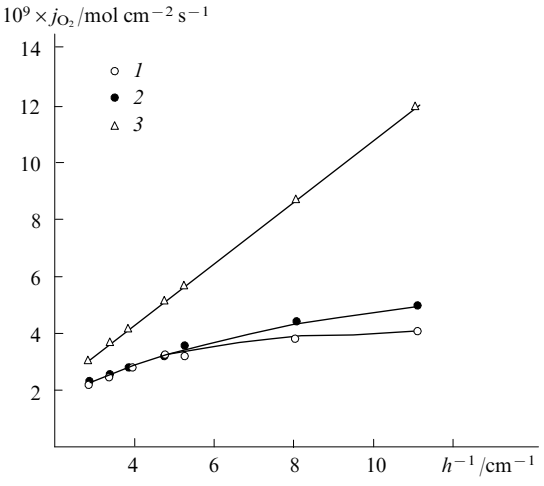


Figure 18. Oxygen flux plotted *vs.* thickness of the molten oxide LGBS composite $BiVO_4$–10 mass % V_2O_5: experimental data (*1*) and results of calculations using Eqn (42) (*2*) and Eqn (37) (*3*).[102] $\log(P'_{O_2}/P''_{O_2}) = 2.3$, $T = 923$ K.

where t_e is the electron transport number, D_i is the diffusion coefficient of oxygen ions and K is the surface exchange coefficient of oxygen. Evaluation of the characteristic thickness of the molten oxide LGBS membrane material $BiVO_4$–10 mass % V_2O_5 gave a value of about 0.07 cm.[102] The curve calculated using expression (42) with $h_c \sim 0.07$ cm and the experimental curve in Fig. 18 almost coincide in the thickness interval of 0.1–0.3 cm. A further decrease in the film thickness (< 0.07 cm) will lead to the situation where the oxygen transport rate will only be controlled by the surface exchange reactions.

Thus, the oxygen flux through the molten oxide LGBS membrane materials $NiO-Bi_2O_3$, $In_2O_3-Bi_2O_3$, $Co_3O_4-Bi_2O_3$ and $ZrV_2O_7-V_2O_5$ at 1023–1173 K is controlled by coupled chemical diffusion (in the experimentally used thickness interval of 0.1–0.3 cm). The exception is only the molten oxide LGBS membrane material $BiVO_4-V_2O_5$ where the oxygen flux is controlled by both chemical diffusion and surface exchange reactions (mixed control). As applied to the molten oxide LGBS membrane materials, this is observed only at temperatures below 973 K.

Table 2. Transport properties of ceramic and molten oxide membrane materials.

Membrane material	T/K	j_{O_2} /mol cm^{-2} s^{-1}	h/mm	P'_{O_2} /MPa	P''_{O_2} /MPa	$j^*_{O_2}$ /mol cm^{-2} s^{-1}	Ref.
Ceramic materials							
$Pr_{0.6}Sr_{0.4}Co_{0.5}Fe_{0.5}O_{3-\delta}$	1173	2.3×10^{-7}	0.6	0.021	0.0001	2.6×10^{-9}	104
$Ba_{0.5}Sr_{0.5}Co_{0.8}Fe_{0.2}O_{3-\delta}$	1173	1.1×10^{-6}	1.2	0.021	0.00065	3.8×10^{-8}	105
$La_{0.6}Ca_{0.4}Co_{0.5}Fe_{0.2}O_{3-\delta}$	1173	1.2×10^{-7}	1.0	0.020	0.00053	3.3×10^{-9}	106
In_2O_3–55 mass % Bi_2O_3	1073	5.3×10^{-8}	2.9	0.021	0.0054	1.1×10^{-8}	79
Molten oxide materials							
In_2O_3–48 mass % Bi_2O_3	1123	8.7×10^{-8}	2.6	0.021	0.0038	1.3×10^{-8}	95
Co_3O_4–36 mass % Bi_2O_3	1123	1.9×10^{-7}	2.0	0.021	0.0047	2.5×10^{-8}	17

To compare the performance of different ion transport membrane materials for oxygen separation, one should determine the specific oxygen permeation rate ($j^*_{O_2}$), or the oxygen permeability

$$j^*_{O_2} = j_{O_2} \frac{h}{\ln(P'_{O_2}/P''_{O_2})} \quad (44)$$

This expression was used to calculate the $j^*_{O_2}$ values only for those membrane materials that exhibit high rate of surface exchange reactions (Table 2).[103] As can be seen, the oxygen permeabilities of the molten oxide LGBS membrane materials and those of the best ceramic membrane materials are comparable.

IV.4. Selectivity

Molten oxide LGBS membrane materials exhibit very high oxygen selectivity.[17] A chromatogram in Fig. 19 *a* confirms high oxygen selectivity of the molten oxide LGBS membrane material Co_3O_4 – 36 mass % Bi_2O_3. According to this chromatogram, the nitrogen flux through the material is almost zero, *i.e.*, $j_{O_2}/j_{N_2} \to \infty$. Assuming that the nitrogen concentration in the permeate flux is beyond the sensitivity limit of the gas chromatograph (10^{-8} g ml^{-1}), the oxygen selectivity of the membrane material in question is estimated at $j_{O_2}/j_{N_2} > 10^5$. So high oxygen selectivity is possible if nitrogen present in air is not dissolved in the molten oxide responsible for the gas tightness of the membrane material.

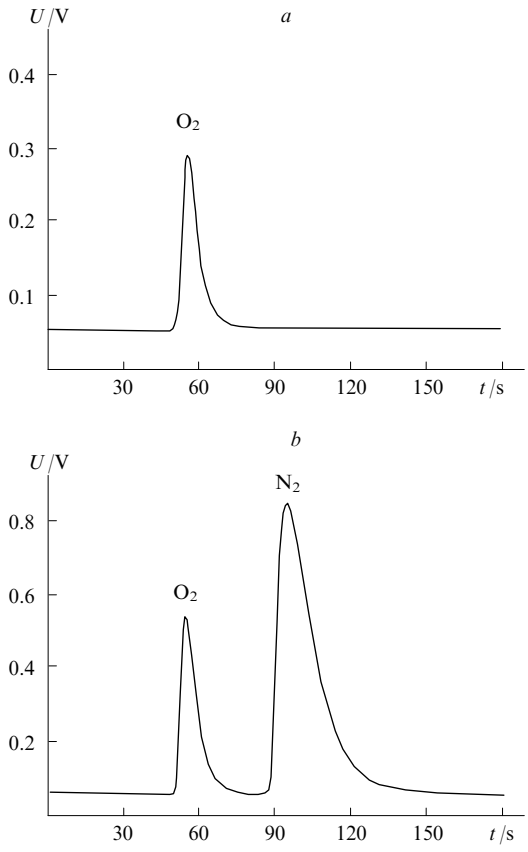


Figure 19. Chromatogram of the gas permeation flux of the molten oxide LGBS composite Co_3O_4 – 36 mass % Bi_2O_3 at 1083 K (*a*) and chromatogram of the gas permeation flux of the ceramic composite Co_3O_4 – 36 mass % Bi_2O_3 at 973 K(*b*).[17]

Thus, the molten oxide LGBS membrane material Co_3O_4 – 36 mass % Bi_2O_3 exhibits high oxygen selectivity and permeability (see Fig. 19, Table 2) and can therefore be used in separators for producing ultrahigh purity oxygen for micro- and nanoelectronics, biotechnology, pharmaceutical industry and other fields of science and technology.

V. Molten oxide fuel cells

Fuel cells convert chemical energy to electricity with high efficiency and no environmental pollution. Usually, fuel cells are classified with respect to electrolyte. There are two classes of fuel cells, *viz.*, high-temperature and low-temperature (main types of fuel cells are characterized in Table 3).[107,108] High-temperature solid-oxide fuel cells have efficiencies of nearly 70% and are therefore of considerable interest for practice. Traditionally, solid-oxide fuel cells operate in the temperature interval of 1073 – 1273 K. High operating temperature accelerates the degradation of electrolytes and electrode materials used in the fuel cells. To solve the problem, the operating temperature should be reduced to 773 – 1073 K; however, this is accompanied by a significant decrease in the ionic conductivity of the electrolytes for the solid-oxide fuel cells (YSZ, GDC, *etc.*) and in the rates of electrode reactions.

In the last decade, much research efforts were aimed to search for novel materials with high oxygen ion conductivity at 773 – 1073 K.[109–114] For instance, Zhu *et al.*[112] proposed a composite electrolyte 'solid GDC – eutectic melt Li_2CO_3 – Na_2CO_3 – K_2CO_3' having high oxygen ion conductivity at 873 K. However, application of this electrolyte in fuel cells is difficult because a mixture of CO_2 and O_2 is required as cathode gas. To solve the problem, a concept of molten oxide fuel cell with air as cathode gas was proposed. An air/chromel/MOE/chromel/CO fuel cell was fabricated;[15] here MOE is the molten oxide LGBS electrolyte TeO_2 – 16 mass % $Te_4Bi_2O_{11}$ consisting of solid TeO_2 grains (dark areas in Fig. 20) and oxygen-ion-conducting intergranular liquid channels (light areas in Fig. 20). Since solid TeO_2 grains do not conduct oxygen ions, the ionic conductivity in the MOE was strongly limited by the content of the liquid phase (recall that from mechanical strength considerations the volume fraction of the liquid phase in the molten oxide material should not exceed 30 vol.% – 35 vol.%).

Recently, a highly conductive molten oxide LGBS electrolyte δ-Bi_2O_3 – 0.2 mass % B_2O_3 was developed; here, both solid δ-Bi_2O_3 grains and intergranular liquid channels conduct oxygen ions.[16] The conductivity of this composite is plotted *vs.* temperature in Fig. 21. This dependence exhibits three characteristic temperature intervals, namely, 823 – 898, 898 – 1003 and 1003 – 1053 K. According to the phase diagram of the Bi_2O_3 – B_2O_3 system,[115] the first temperature interval corresponds to the conductivity of ceramic composite α-Bi_2O_3 – $Bi_{24}B_2O_{39}$. The kink at 898 K in the conductivity curve is due to peritectic decomposition of $Bi_{24}B_2O_{39}$ and formation of the molten oxide LGBS composite α-Bi_2O_3 – 0.2 mass % B_2O_3. Therefore, the second temperature interval corresponds to the conductivity of this composite. The conductivity jump at 1003 K is due to the polymorphic transformation α-Bi_2O_3 → δ-Bi_2O_3; it is accompanied by abrupt increase in the oxygen ion conductivity.[98–100] Thus, the third temperature interval corresponds to the conductivity of the molten oxide LGBS

Table 3. Fuel cell types.[108]

Fuel cell	T/K	Anode reaction	Cathode reaction	Charge carrier in electrolyte
AFC	<373	$H_2 + 2HO^- \longrightarrow 2H_2O + 2e^-$	$1/2O_2 + H_2O + 2e^- \longrightarrow 2HO^-$	HO^-
PEMFC	333–393	$H_2 \longrightarrow 2H^+ + 2e^-$	$1/2O_2 + 2H^+ + 2e^- \longrightarrow H_2O$	H^+
DMFC	333–393	$MeOH + H_2O \longrightarrow CO_2 + 6H^+ + 6e^-$	$3/2O_2 + 6H^+ + 6e^- \longrightarrow 3H_2O$	H^+
PAFC	433–493	$H_2 \longrightarrow 2H^+ + 2e^-$	$1/2O_2 + 2H^+ + 2e^- \longrightarrow H_2O$	H^+
MCFC	873–1073	$H_2 + CO_3^{2-} \longrightarrow H_2O + CO_2 + 2e^-$	$1/2O_2 + CO_2 + 2e^- \longrightarrow CO_3^{2-}$	CO_3^{2-}
SOFC	1073–1273	$H_2 + O^{2-} \longrightarrow H_2O + 2e^-$	$1/2O_2 + 2e^- \longrightarrow O^{2-}$	O^{2-}

Note. Fuel cell (FC) notations are as follows: AFC is Alkaline, PEMFC is Polymer Electrolyte Membrane, DMFC is Direct Methanol, PAFC is Phosphoric Acide, MCFC is Molten Carbonate, SOFC is Solid Oxide.

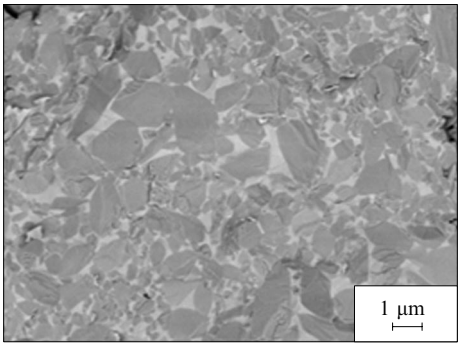


Figure 20. Microstructure (fracture face) of the molten oxide LGBS composite TeO_2–16 mass % $Te_4Bi_2O_{11}$ after cooling from 913 K.[15]

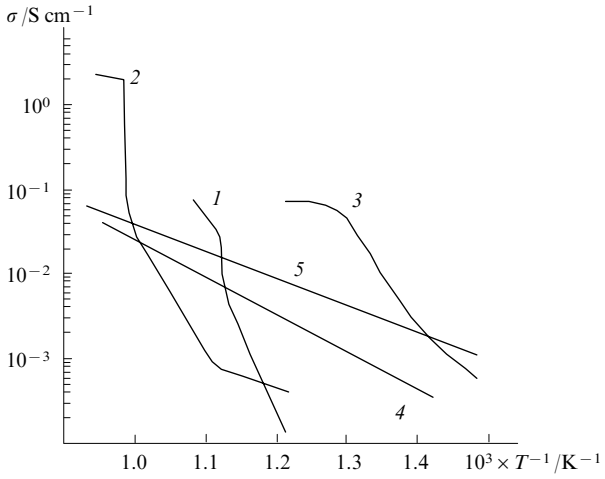


Figure 21. Conductivities of molten oxide electrolytes (*1*, *2*) and conventional electrolytes (*3*–*5*) plotted *vs.* temperature.[16] TeO_2–16 mass % Bi_2O_3 (*1*), δ-Bi_2O_3–0.2 mass % B_2O_3 (*2*), $Ce_{0.8}Sm_{0.2}O_{1.9}$–50 vol.% $Li_{0.62}K_{0.38}CO_3$ (*2*), 8 YSZ (*4*) and $Ce_{0.9}Gd_{0.1}O_{2-\delta}$ (*5*).

composite δ-Bi_2O_3–0.2 mass % B_2O_3. The oxygen ion transport number of this composite determined by the volumetric measurements of the faradaic efficiency technique [16] was 0.96 ± 0.03 at 1023 K. This confirms high oxygen ion conductivity of the composite in the temperature interval of 1003–1053 K. The ionic conductivity of the composite is governed by both the solid phase δ-Bi_2O_3 and the intergranular liquid channels; it cannot be ruled out that the solid δ-Bi_2O_3/melt interfaces also contribute to the ionic conductivity.[116, 117]

For comparison, Table 4 lists the performance characteristics of different fuel cells including the molten oxide ones. As can be seen, the molten oxide fuel cells are characterized by high current density and low operating voltage, which seems to be due to the low decomposition potential of the oxides Bi_2O_3 and TeO_2 as components of the molten oxide electrolytes. In the future, it is of interest to study the transport properties of the molten oxide LGBS electrolytes YSZ–B_2O_3 and GDC–B_2O_3 with higher decomposition potentials.

VI. Modelling. The dynamic polymer chain model

A key issue to the membrane and electrolyte materials considered in this review concerns the mechanism of oxygen

Table 4. Performance characteristics of fuel cells.

Electrolyte	I/mA cm^{-2}	U/V	h/mm	T/K	Ref.
$Ce_{0.8}Sm_{0.2}O_{1.9}$–20 mass % (Li_2CO_3–33 mol.% Na_2CO_3)	480	0.52	0.3	633	118
α-$LiAlO_2$–50 vol.% (Li_2CO_3–38 mol.% K_2CO_3)	150	0.85	0.3	923	113
$Ce_{0.8}Sm_{0.2}O_{1.9}$–30 mass % (Li_2CO_3–31.5 mol.% Na_2CO_3–25 mol.% K_2CO_3)	1300	0.55	0.5	923	119
TeO_2–16 mass % $Te_4Bi_2O_{11}$	720	0.13	0.3	923	15
δ-Bi_2O_3–0.2 mass % B_2O_3	1550	0.17	0.5	1023	120

ion transport in molten oxides. Recently, a number of models for mass transport in molten oxides have been proposed.[22, 121–123] In particular, the dynamic polymer chain model describes the oxygen ion transport in the molten oxides based on V_2O_5.[22] Prior to discussing the model, we will briefly outline the structure of melts.

The structures of molten V_2O_5 and binary systems based on it were studied by X-ray and neutron diffraction, NMR spectroscopy, Raman spectroscopy, *etc.*[124–134] It was established that melting of V_2O_5 causes the intramolecular coordination of atoms to change insignificantly. Nevertheless, some of weak bonds V–O break and chains of distorted tetrahedra VO_4 or trigonal bipyramids VO_5 are formed, as in the glassy oxides based on V_2O_5 (Fig. 22). The average number of structural units in the chain depends on the temperature, being equal to 120 at 973 K.[133]

The structure of oxide glasses based on Bi_2O_3 was intensively studied by X-ray diffraction, atomic absorption spectroscopy, Raman spectroscopy, IR spectroscopy, electron paramagnetic resonance, *etc.*[135–144] It was shown that glassy Bi_2O_3 forms trigonal pyramids BiO_3 or distorted octahedra BiO_6. Based on IR spectroscopy data, Milanova *et al.*[144] proposed that the structure of glassy bismuth oxide can also be built of BiO_n polyhedra. Taking account of the aforesaid, one can admit the presence of trigonal pyramids BiO_3 or distorted octahedra BiO_6 in the structure of molten Bi_2O_3.

Consider the oxygen ion transport in molten V_2O_5 within the framework of the dynamic polymer chain model. The process is schematically shown in Fig. 23. The key points of the model are as follows:

— the melt has a polymeric structure;

— the average length of the polymer chain is temperature dependent;

— breakdown and connection of polymer chains in the melt occur stochastically and isentropically;

— breakdown of a polymer chain causes the formation of two chains with a terminal oxygen pseudovacancy in one of them;

— chain connection is followed by release of one of two terminal oxygen ions;

— the free oxygen ion is trapped by the nearest pseudovacancy;

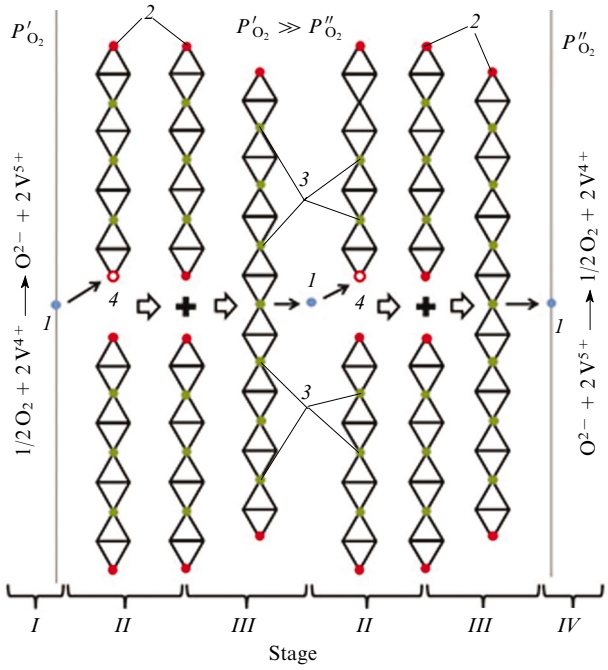


Figure 23. Oxygen ion transport in molten V_2O_5: a schematic.[68] Mobile oxygen (*1*), terminal oxygen (*2*), bridging oxygen (*3*) and oxygen pseudovacancy (*4*).

— transport of oxygen ions and electrons through the melt is driven by the electrochemical potential gradient;

— the relative migration rates of oxygen anions and electrons are balanced so the total charge transferred is zero.

The oxygen ion transport in molten V_2O_5 within the framework of this model is schematically shown in Fig. 23. An oxygen ion chemisorbed on the melt surface (stage *I*) is trapped by the nearest terminal pseudovacancy. As a result, a terminal oxygen is formed (stage *II*). The subsequent chain connection results in the formation of a free oxygen ion (stage *III*), which is trapped by the nearest pseudovacancy, *etc.* Eventually, the free oxygen ion arrives at the

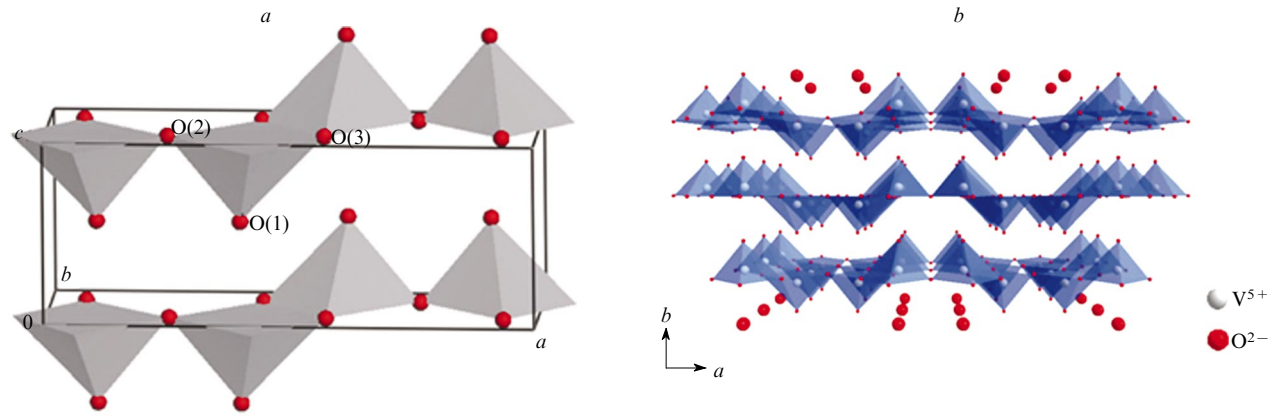


Figure 22. Structure of V_2O_5:[122] melt (*a*) and crystal (*b*).

opposite melt surface (stage *IV*). The electronic conductivity of the melt is provided by vanadium

$$V^{5+} + e^- \longrightarrow V^{4+} \quad (44a)$$

In accordance with the model, there is one oxygen pseudovacancy per two chains, each containing N metal atoms and $xN/2$ oxygen atoms (x is the oxidation state of the metal). Thus, the concentration of oxygen pseudovacancies (c_i) or mobile oxygen ions, is xN times lower than the concentration of oxygen atoms in the molten oxide (c_m)

$$c_i = \frac{c_m}{xN} \quad (45)$$

The concentration of oxygen atoms is given by

$$c_m = \frac{x\rho}{2M} \quad (46)$$

where ρ and M are the density and molar mass of the molten oxide, respectively. Substituting Eqn (46) into relation (45), one gets the following expression for the concentration of charge carriers:

$$c_i = \frac{\rho}{2MN} \quad (47)$$

The oxygen ion conductivity in the melt is given by

$$\sigma_i = B_i z_i c_i F \quad (48)$$

In accordance with the Nernst–Einstein equation,

$$B_i = \frac{D_i z_i^2 F}{RT} \quad (49)$$

where D_i is the diffusion coefficient of oxygen ions in the melt. Substituting Eqn (49) into Eqn (48) gives the following expression for the ionic conductivity:

$$\sigma_i = \frac{D_i c_i z_i^2 F^2}{RT} \quad (50)$$

Since the liquid phase percolates in the molten oxide membrane materials (see Figs 8, 9, 20), their oxygen ion conductivity (σ_i^*) can be expressed as follows:

$$\sigma_i^* = \eta\sigma_i \quad (51)$$

where η is the volume fraction of the liquid phase in the molten oxide membrane material. Using Eqns (38), (47), (50) and (51), one gets the expression for the oxygen flux through the molten oxide membranes:

$$j_{O_2} = \frac{\rho\eta D_i}{8MNh}\ln\left(\frac{P'_{O_2}}{P''_{O_2}}\right) \quad (52)$$

Experimental j_{O2} values and the results of calculations using formula (52) for the molten oxide membranes based on V_2O_5 ($N = 120$) (Ref. 22) and Bi_2O_3 ($N = 1$) (Ref. 145) are in order-of-magnitude agreement, thus confirming the correctness of the model.

* * *

Our analysis of published data revealed some recent advances in the design of novel molten oxide electrochemical materials. Based on the results obtained, these materials may find application in electrochemical devices for power generation and oxygen production for various fields from power engineering to nanoelectronics and biotechnology. However, studies on these materials raised a number of issues that should be clarified. In particular, ideas about the mechanisms of oxygen ion transport in molten oxides are underdeveloped. The mechanical properties of molten oxide materials have been poorly studied so far. This makes the assessment of their potential for technological applications difficult. Specific features of the influence of the solid oxide/liquid oxide interfaces on the transport properties of molten oxide materials are unascertained. The formation of space charge regions with high ionic conductivity near interfaces was reported.[116, 117] In this connection, the concept of liquid-channel grain-boundary nanostructure[34] offers great prospects for the design of molten oxide nanomaterials with oxygen ion conductivity.

The author expresses his gratitude to Ph.D. (Chem.) S.V.Fedorov, Ph.D. (Chem.) A.A.Klimashin and Ph.D. (Chem.) I.V.Kulbakin for useful tips in discussing the material.

The review has been written with the financial support from the Russian Science Foundation (Project No. 16-19-10608).

References

1. V S Arutyunov, G V Lisichkin *Russ. Chem. Rev.* **86** 777 (2017)
2. V S Bagotsky, A M Skundin, Y M Volfkovich *Electrochemical Power Source: Batteries, Fuel Cells, and Supercapacitors* (Wiley, 2015)
3. N Mahato, A Banerjee, A Gupta, S Omar, K Balani *Prog. Mater. Sci.* **72** 141 (2015)
4. V L Kozhevnikov, I A Leonidov, I V Patrakeev *Russ. Chem. Rev.* **82** 772 (2013)
5. S R Bishop, D Marrocchelli, C Chatzichristodoulou, N H Perry, M B Mogensen, H L Tuller, E D Wachsman *Annu. Rev. Mater. Res.* **44** 205 (2014)
6. A Atkinson, J Kilner, S Skinner, N Brandon, D J L Brett *Intermediate-Temperature Solid Oxide Fuel Cells. Encyclopedia of Inorganic Chemistry* (Wiley, 2011)
7. Z Gao, L V Mogni, E C Miller, J G Railsback, S A Barnett *Energy Environ. Sci.* **9** 1602 (2016)
8. E D Wachsman, K T Lee *Science* **334** 935 (2011)
9. A Chroneos, B Yildiz, A Tarancon, D Parfitt, J A Kilner *Energy Environ. Sci.* **4** 2774 (2011)
10. S Ya Istomin, E V Antipov *Russ. Chem. Rev.* **82** 686 (2013)
11. A B Yaroslavtsev *Russ. Chem. Rev.* **85** 1255 (2016)
12. L M Kolchina, N V Lyskov, A N Kuznetsov, S M Kazakov, M Z Galin, A Meledin, A M Abakumov, S I Bredikhin, G N Mazo, E V Antipov *RSC Adv.* **6** 101029 (2016)
13. M P Popov, I A Starkov, S F Bychkov, A P Nemudry *J. Membr. Sci.* **469** 1306 (2014)
14. V V Belousov *Acc. Chem. Res.* **50** 273 (2017)
15. V V Belousov, S V Fedorov *Fuel Cells,* **16** 401 (2016)
16. V V Belousov, S V Fedorov *Chem. Commun.* **53** 565 (2017)
17. V V Belousov, I V Kulbakin, S V Fedorov, A A Klimashin *ACS Appl. Mater. Interfaces,* **8** 22324 (2016)
18. V V Belousov *J. Am. Ceram. Soc.* **79** 1703 (1996)

19. V V Belousov *MRS Commun.* **3** 225 (2013)
20. V V Belousov *Oxid. Met.* **42** 511 (1994)
21. S V Fedorov, V V Belousov, A V Vorobiev *J. Electrochem. Soc.* **155** F241 (2008)
22. V V Belousov, A A Klimashin, S V Fedorov *Ionics* **22** 369 (2016)
23. J W Cahn *J. Chem. Phys.* **66** 3667 (1977)
24. M R Moldover, J W Cahn *Science* **207** 1073 (1980)
25. G F Teletzke, L E Scriven, H T Davis *J. Chem. Phys.* **77** 5794 (1982)
26. V V Belousov *Kolloid. Zh.* **66** 149 (2004)
27. R H French *J. Am. Ceram. Soc.* **83** 2117 (2000)
28. V V Belousov, S V Fedorov *Russ. Chem. Rev.* **81** 44 (2012)
29. J P Gambino, W D Kingery, G E Pike, L M Levinson, H R Phillip *J. Am. Ceram. Soc.* **72** 642 (1989)
30. P R Cantwell, M Tang, S J Dillon, J Luo, G S Rohrer, M P Harmer *Acta Mater.* **62** 1 (2014)
31. M Fujimoto, W D Kingery *J. Am. Ceram. Soc.* **68** 169 (1985)
32. V V Belousov *J. Am. Ceram. Soc.* **82** 1342 (1999)
33. J Luo, Y-M Chiang *Acta Mater.* **48** 4501 (2000)
34. V V Belousov *JETP Lett.,* **88** 259 (2008)
35. W T Read, W Shockley *Phys. Rev.* **78** 275 (1950)
36. C Kittel *Introduction to Solid State Physics* (New York: Wiley, 1975)
37. R J Hunter *Foundations of Colloid Science* (Oxford: Oxford University Press, 2002)
38. D R Clarke *J. Am. Ceram. Soc.* **70** 15 (1987)
39. B V Derjaguin *Theory of Stability of Colloids and Thin Films* (Springer, 1989)
40. B V Derjaguin, N V Churaev, V M Muller *Surface Forces* (New York: Plenum, 1987)
41. K Berland, V R Cooper, K Lee, E Schroder, T Thonhauser, P Hildgard, B I Lundquist *Rep. Prog. Phys.* **78** 066501 (2015)
42. I E Dzyaloshinskii, E M Lifshits, L P Pitaevskii *Usp. Fiz. Nauk* **73** 381 (1961)
43. V L Ginzburg, L D Landau *Zh. Eksp. Teoret. Fiz.* **20** 1064 (1950)
44. J W Cahn, J E Hillard *J. Chem. Phys.* **28** 258 (1958)
45. V V Belousov, A A Klimashin *Metall. Mater. Trans. A* **43** 3715 (2012)
46. V V Belousov, A A Klimashin *Russ. Chem. Rev.* **82** 273 (2013)
47. A A Klimashin, V V Belousov *Corros. Sci.* **53** 3150 (2011)
48. A A Klimashin, V V Belousov *Oxid. Met.* **76** 359 (2011)
49. V V Belousov *Russ. J. Phys. Chem. A.* **82** 79 (2008)
50. V V Belousov *Russ. Chem. Rev.* **67** 563 (1998)
51. N Birks, G H Meier, F S Pettit *Introduction to the High-Temperature Oxidation of Metals* (Cambridge: Cambridge University Press, 2006)
52. H Singh, D Puri, S Prakash *Rev. Adv. Mater. Sci.* **16** 27 (2007)
53. T S Sidhu, S Prakash, R D Agrawal *Corros. Sci.* **90** 41 (2006)
54. R A Rapp *Corros. Sci.* **44** 209 (2002)
55. W Gao, Z Li *Developments in High Temperature Corrosion and Protection of Materials* (Cambridge: Publishing Limited, 2008)
56. D J Young *High Temperature Oxidation and Corrosion of Metals* (Oxford: Elsevier, 2008)
57. M Kutz *Handbook of Environmental Degradation of Materials* (Norwich, NY: William Andrew Publishing, 2005)
58. X Montero, M C Galetz *Oxid. Met.* **83** 485 (2015)
59. J Porcay-Calderon, V M Salinas-Bravo, R A Rodriguez-Diaz, L Martinez-Gomez *Int. J. Electrochem. Sci.* **10** 4928 (2015)
60. R A Rapp, N Otsuka *ECS Trans.* **16** 271 (2009)
61. W-Y Zhao, B-W Xu, Y Ma, S-K Gong *Prog. Nat. Sci.: Mater. Int.* **21** 322 (2011)
62. N Eliaz, G Shemesh, R M Latanision *Eng. Fail. Anal.* **9** 31 (2002)
63. B Haltstedt, D Risold, L J Gauckler *J. Am. Ceram. Soc.* **79** 353 (1996)
64. M P Kulakov, D Ya Lenchinenko *Thermochim. Acta* **188** 129 (1991)
65. N V Lyskov, Yu G Metlin, V V Belousov, Yu D Tretyakov *Solid State Ionics* **166** 207 (2004)
66. N V Lyskov, Yu G Metlin, V V Belousov, Yu D Tretyakov *Solid State Ionics* **173** 135 (2004)
67. V V Belousov *Corros. Sci.* **52** 68 (2010)
68. V V Belousov *Ionics* **22** 451 (2016)
69. C Wagner *Z. Electrochem.* **60** 4 (1956)
70. J E ten Elshof, H J M Bouwmeester, H Verweij *Solid State Ionics* **81** 97 (1995)
71. H J M Bouwmeester, A J Burggraaf, in *The CRC Handbook of Solid State Electrochemistry* (Eds P J Gellings, H J M Bouwmeester) (New York: CRC Press, 1997) p. 481
72. M A Pesa, J L G Fierro *Chem. Rev.* **101** 1981 (2001)
73. T J Mazanec, T L Cable, J G Frye Jr *Solid State Ionics* **53 – 56** 111 (1992)
74. T J Mazanec *Solid State Ionics* **70 – 71** 11 (1994)
75. K Huang, M Schroeder, J B Goodenough *Electrochem. Solid-State Lett.* **2** 375 (1999)
76. E Ruiz-Trejo, P Boldrin, A Lubin, F Tariq, S Fearn, R Chater, S N Cook, A Atkinson, R I Gruar, C J Tighe, J Darr, N P Brandon *Chem. Mater.* **26** 3887 (2014)
77. E Capoen, M C Steil, G Nowogrocki, M Malys, C Pirovano, A Lifberg, E Bordes-Richard, J C Boivin, G Mairesse, R N Vannier *Solid State Ionics* **177** 483 (2006)
78. E Capoen, G Nowogrocki, R J Chater, S J Skinner, J A Kilner, M Malys, J C Boivin, G Mairesse, R N Vannier *Solid State Ionics* **177** 489 (2006)
79. V V Belousov, V A Schelkunov, S V Fedorov, I V Kul'bakin, A V Vorobiev *Electrochem. Commun.* **20** 60 (2012)
80. V V Belousov, V A Schelkunov, S V Fedorov, I V Kulbakin, A V Vorobiev *Ionics* **18** 787 (2012)
81. Y Lin, S Fang, D Su, K S Brinkman, F Chen *Nat. Commun.* **6** 6824 (2015)
82. Z Zhang, W Zhou, Y Chen, D Chen, J Chen, S Liu, W Jin, Z Shao *ACS Appl. Mater. Interfaces* **7** 22918 (2015)
83. M Sasabe, K S Goto *Metall. Trans.* **5** 2225 (1974)
84. M Sasabe, J Masami *Can. Metall. Quart.* **22** 29 (1983)
85. Y Sayadyaghoubi, S Sun, S Jahanshahi *Metall. Mater. Trans. B* **26** 795 (1996)
86. V V Belousov *Metall. Mater. Trans. A* **45** 4257 (2014)
87. V R Yarlagadda, T V Nguyen *ECS Trans.* **33** 119 (2011)
88. V A M Brabers, A D D Broemme *J. Magn. Magn. Mater.* **104 – 107** 405 (1992)
89. M Chen, B Hallsted, L J Gauckler *J. Phase Equilib.* **24** 212 (2003)
90. H St C O'Neill *Phys. Chem. Miner.* **12** 149 (1985)
91. I V Kul'bakin, V V Belousov, S V Fedorov, A V Vorobiev *Mater. Lett.* **67** 139 (2012)
92. E M Levin, R S Roth *J. Res. Natl. Bur. Stand.* 68A 189 (1964)
93. D C Craig, N C Stephenson *J. Solid State Chem.* **15** 1 (1975)
94. A Janotti, C G Van de Walle *Rep. Prog. Phys.* **72** 126501 (2009)
95. V V Belousov, S V Fedorov, I V Kul'bakin *J. Membr. Sci. Res.* **1** 96 (2015)
96. T Bak, J Nowotny, M Rekas, C C Sorrell, P A Banda, W Wlodarski *J. Mater. Sci.* **13** 571 (2002)
97. J Feinleib, D Adler *Phys. Rev. Lett.* **21** 1010 (1968)
98. H A Harwig, A G Gerards *J. Solid State Chem.* **26** 265 (1978)
99. P D Battle, C R A Catlow, J Drennan, A D Murray *J. Phys., C* **16** L561 (1983)
100. S Hull *Rep. Prog. Phys.* **67** 1233 (2004)
101. H J M Bouwmeester, H Kruidhof, A J Burggraaf *Solid State Ionics* **72** 185 (1994)
102. V V Belousov, S V Fedorov, A V Vorobiev *J. Electrochem. Soc.* **158** B601 (2011)

103. A S Yu, J M Vohs, R J Gorte *Energy Environ. Sci.* **7** 944 (2014)
104. K Partovi, F Liang, O Ravkina, J Caro *ACS Appl. Mater. Interfaces* **6** 10274 (2014)
105. P Zeng, Z Chen, W Zho, H Gu, Z Shao, S Liu *J. Membr. Sci.* **291** 148 (2007)
106. K Efimov, T Klande, N Juditzki, A Feldhoff *J. Membr. Sci.* **389** 205 (2012)
107. B C H Steele, A Heinzel *Nature (London)* **414** 345 (2001)
108. L Carrette, K A Friedrich, U Stimming *ChemPhysChem* **1** 162 (2000)
109. E Antolini *Appl. Energy* **88** 4274 (2011)
110. J B Goodenough, P Singh *J. Electrochem. Soc.* **162** A2387 (2015)
111. J A Kilner, M Burriel *Annu. Rev. Mater. Res.* **44** 365 (2014)
112. W Zhu, C Xia, D Ding, X Shi, G Meng *Mater. Res. Bull.* **41** 2057 (2006)
113. C Xia, Y Li, Y Tian, Q Liu, Y Zhao, L Jia, Y Li *J. Power Sources* **188** 156 (2009)
114. C Xia, Y Li, Y Tian, Q Liu, Z Wang, L Jia, Y Zhao, Y Li *J. Power Sources* **195** 3149 (2010)
115. E M Levin, C L McDaniel *J. Am. Ceram. Soc.* **45** 355 (1962)
116. V V Belousov *J. Eur. Ceram. Soc.* **27** 3459 (2007)
117. A Chandra, J Maier *Solid State Ionics* **148** 153 (2002)
118. B Zhu, X T Yang, J Xu, Z G Zhu, S J Ji, M T Sun, J C Sun *J. Power Sources* **118** 47 (2003)
119. H-J Choi, J-J Lee, S-H Hyun, H-C Lim *Int. J. Hydrogen Energy* **36** 11048 (2011)
120. V V Belousov *ECS Trans.* (2017) (in the press)
121. A A Klimashin, V V Belousov *Metall. Mater. Trans. B* **47** 749 (2016)
122. A A Klimashin, V V Belousov *Russ. J. Phys. Chem. A* **90** 54 (2016)
123. E Thibodeau, I H Jung *Metall. Mater. Trans. B* **47** 355 (2016)
124. H Morikawa, M Miyake, S-I Iwai, K Furukawa, A Revcolevschi *J. Chem. Soc., Faraday Trans.* **77** 361 (1981)
125. L Leontiev, V Boronenkov, M Zinigrad, E Pastukhov, M Shalimov, S Shanshurov *Phase Interaction in the Metal–Oxide Melts–Gas Systems: The Modeling of Structure, Properties, and Processes* (Berlin: Springer, 2011)
126. N A Vatolin, E A Pastukhov *Difraktsionnye Issledovaniya Stroeniya Vysokotemperaturnykh Rasplavov* (Diffraction Studies of the Structure of High-Temperature Melts) (Moscow: Nauka, 1980)
127. O A Esin, V L Zyazev *Zh. Neorg. Khim.* **2** 1998 (1957)
128. V I Musikhin, E A Pastukhov, N A Vatolin, B M Lepinskikh *Neorg. Mater.* **7** 99 (1971)
129. E A Pastukhov, V I Musikhin, N A Vatolin *Elektricheskie Svoistva Nestekhiometricheskikh Oksidnykh Rasplavov* (Electrochemical Properties of Nonstoichiometric Oxide Melts) (Sverdlovsk: Ural Scientific Centre, Academy of Sciences of the USSR, 1984)
130. P P Arsent'ev, V V Yakovlev, M G Krasheninnikov, L A Pronin, E S Filippov *Fiziko-Khimicheskie Metody Issledovaniya Metallurgicheskikh Protsessov* (Physicochemical Methods of Investigation of Metallurgical Processes) (Moscow: Metallurgiya, 1988)
131. S Takeda, Y Kawakita, M Inui, K Maruyama, S Tamaki, K Sugiyama, Y Waseda *J. Non-Cryst. Solids* **205–207** 151 (1996)
132. N A Vatolin *Rasplavy* (1) 5 (1987)
133. V M Mastikhin, O B Lapina, L G Simonova *Rasplavy* (2) 21 (1990)
134. O A Esin, V P Gel'd *Fizicheskaya Khimiya Pirometallurgicheskikh Protsessov* (Physical Chemistry of Pyrometallurgical Processes) (Moscow: Metallurgiya, 1966)
135. P Fleury *C.R. Acad. Sci. Paris Ser. C* **263** 1375 (1966)
136. M F Mal'tseva, A A Fotiev *Zh. Neorg. Khim.* **23** 1096 (1978)
137. H Doweidar *J. Non-Cryst. Solids* **404** 49 (2014)
138. L Baia, R Stefan, W Kiefer, S Simon *J. Raman Spectrosc.* **36** 262 (2005)
139. Ch Srinivasu, Ch Mallika, G Sriramulu, A Hameed, A Edukondalu *Int. J. Sci. Eng. Res.* **5** 263 (2014)
140. I Ardelean, S Cora, D Rusu *Physica B* **403** 3682 (2008)
141. G Zhao, Y Tian, H Fan, J Zhang, L Hu *J. Mater. Sci. Technol.* **29** 209 (2013)
142. S Hazra, A Ghosh *Phys. Rev. B* **51** 851 (1995)
143. S Hazra, S Mandal, A Ghosh *Phys. Rev. B* **56** 8021 (1997)
144. M Milanova, R Iordanova, Y Dimitriev, K L Kostov *Phys. Chem. Glasses: Eur. J. Glass Sci. Technol. B* **48** 255 (2007)
145. A A Klimashin, V V Belousov *J. Electrochem. Soc.* **164** H5353 (2017)